Wind and turbulence observations with the Mars microphone on Perseverance

Alexander E. Stott[1], Naomi Murdoch[1], Martin Gillier[1], Don Banfield[2], Tanguy Bertrand[3], Baptiste Chide[4], Manuel De la Torre Juarez[5], Ricardo Hueso[6], Ralph Lorenz[7], German Martinez[8,9], Asier Munguira[6], Luis Mora Sotomayor[10], Sara Navarro[10], Claire Newman[11], Paolo Pilleri[12], Jorge Pla-Garcia[10], Jose Antonio Rodriguez-Manfredi[10], Agustin Sanchez-Lavega[6], Michael Smith[13], Daniel Viudez Moreiras[10], Nathan Williams[5], Sylvestre Maurice[12], Roger C. Wiens[14], David Mimoun[1]

[1]Institut Supérieur de l'Aéronautique et de l'Espace (ISAE-SUPAERO), Université de Toulouse, Toulouse, France.
[2]NASA Ames, Mountain View, CA, USA
[3]Laboratoire d'Etudes Spatiales et d'Instrumentation en Astrophysique (LESIA), Observatoire de Paris-PSL, CNRS, Sorbonne Université, Université de Paris Cité, Meudon, France.
[4]Space and Planetary Exploration Team, Los Alamos National Laboratory, Los Alamos, NM, USA.
[5]Jet Propulsion Laboratory – California Institute of Technology, Pasadena, CA, USA.
[6]Fisica Aplicada, Escuela de Ingeniería de Bilbao, Universidad del País Vasco UPV/EHU, Bilbao, Spain.
[7]Johns Hopkins Applied Physics Lab, Laurel, MD, USA.
[8]Lunar and Planetary Institute, USRA, Houston, TX, USA.
[9]University of Michigan, Ann Arbor, MI, USA.
[10]Centro de Astrobiologia (CAB), CSIC-INTA, Madrid, Spain
[11]Aeolis Research, Chandler, AZ, USA.
[12]Institut de Recherche en Astrophysique et Planétologie (IRAP), Université de Toulouse 3 Paul Sabatier, CNRS, CNES, Toulouse, France.
[13]Goddard Space Flight Center, Greenbelt, MD, USA.
[14]Purdue University, West Lafayette, IN, USA.

Key Points:

- Wind-induced noise is observed by the SuperCam Mars microphone on Perseverance.
- The wind speed can be estimated at high frequencies from the microphone and temperature data using a machine learning model.
- We quantify the relationship between the turbulent intensity of the wind speed and pressure drops, temperature, energy flux and opacity.

Corresponding author: Alexander Stott, `Alexander.stott@isae-supaero.fr`

Abstract

We utilise SuperCam's Mars microphone to provide information on wind speed and turbulence at high frequencies on Mars. This is achieved through a correlation analysis between the microphone and meteorological data which shows that the microphone signal power has a consistent relationship with wind speed and air temperature. A calibration function is constructed using Gaussian process regression (a machine learning technique) to use the microphone signal and air temperature to produce an estimate of the wind speed. This wind speed estimate is at a high rate for in situ measurements on Mars, with a sample every 0.01 s. As a result, we determine the fast fluctuations of the wind at Jezero crater which highlights the nature of wind gusts over the martian day. We evaluate the normalised wind standard deviation (gustiness) on the estimated wind speed to analyse the turbulent behaviour. Correlations are shown between the evaluated gustiness statistic and pressure drop rates, temperature, energy fluxes and optical opacity to characterise the behaviour of high frequency turbulent intensity at Jezero crater. This has implications for future atmospheric models on Mars, taking into account turbulence at the finest scales.

Plain Language Summary

The NASA Perservance mission sent a microphone to the surface of Mars. This microphone has recorded signals due to the wind. We examine how these recorded signals vary with other sensor data from Perseverance, which shows a link between the microphone signal, the dedicated wind speed sensor and air temperature. Based on this finding we develop a way to predict the wind speed from the microphone data using a machine learning technique. The microphone records data at a very high rate for sensors so far sent to Mars. This means that the wind speed predicted from the microphone data can be used to study its chaotic and variable behaviour on Mars to a level never seen before. We show that this chaotic and variable behaviour has links to temperature, the amount of dust particles in the atmosphere and the number of whirlwinds observed. This will lead us to better weather models for Mars.

1 Introduction

The NASA Perseverance mission searches for signs of past habitable environments in Jezero crater, part of an ancient delta on Mars (Farley et al., 2020; Mangold et al., 2021), as it also prepares for future human exploration. A large part of this search requires the determination of the dynamic processes currently at play on Mars (Dundas et al., 2021). One major contributor of day to day surface alteration is through aeolian processes, whereby dust and sand are lofted and transported. Such activity ranges from the movement of single particles and local dust lifting in dust devils, to larger scale dust lifting events by wind gusts and even dust storms which can become global (Zurek & Martin, 1993; Wang & Richardson, 2015; Newman et al., 2022; Charalambous, McClean, et al., 2021; Murdoch et al., 2021). The control and variation of these processes is yet to be fully understood, and so, in situ measurements of the dynamic atmospheric environment, particularly turbulence, can yield new insights.

Perseverance provides the first measurements of the Martian soundscape (Maurice et al., 2022; Mimoun et al., 2022). The current catalogue of recordings includes rover noises, the Ingenuity rotorcraft, shock waves from the SuperCam Laser Induced Breakdown spectroscopy (LIBS) technique and the noise of the Martian wind. The propagation and origin of these sounds depend on the properties of the atmosphere and their variation. Notably, these measurements are at a high rate (up to 100 kHz but more usually 25 kHz) and, therefore, they offer a new way to observe the high frequency atmospheric variation on Mars. This high frequency sampling of atmospheric variations is important to characterise stochastic variations in the Planetary Boundary Layer (PBL), in particu-

lar how the energy dissipates at the small scales (Maurice et al., 2022). This turbulent behaviour is linked to dust lifting and so its characterisation is important to understand the ongoing surface change on Mars (Dundas et al., 2021; Newman et al., 2022).

The aim of this work is to use the SuperCam microphone data to characterise the wind speed and its turbulent behaviour at high frequencies. To do so, we first provide a sensitivity analysis of the SuperCam microphone recordings to the properties of the ambient Martian atmosphere. In general the signal is shown to be correlated to wind speed with contributions from the variation in the wind speed (its standard deviation), temperature and pressure variation. We next use these sensitivities to produce a calibration of microphone data to wind speed and so infer a wind speed estimate based on the microphone data. This is achieved though Gaussian process (GP) regression (Williams & Rasmussen, 1995), a machine learning technique. This wind speed estimate represents the highest frequency wind speed measurement obtained on Mars so far. We examine this estimate for a range of atmospheric conditions and present an analysis of its variability in terms of gustiness, a marker of turbulent intensity. We then show how this gustiness metric correlates with measured environmental data from the Perseverance meteorological sensor package (Rodriguez-Manfredi et al., 2021) to define how turbulence in the PBL can be controlled. Moreover, we provide a comparison to pressure drop rates, another marker of turbulence. As a result, we demonstrate how the microphone can be used to extract information on turbulence at high frequencies, shedding light on the PBL dynamics.

2 Background

2.1 The Martian Planetary boundary layer

The PBL is the part of the atmosphere at the interface with the planet surface. This region represents the atmosphere directly affected by the surface and, on Mars, is where heat, momentum, chemical species and dust are mixed with the free atmosphere (Petrosyan et al., 2011; Spiga, 2019). It is therefore, crucial to the overall climate modelling of Mars (Read et al., 2015, 2017).

The thin Martian atmosphere is inefficient at heating and cooling the surface and so during the day the PBL is forced by radiative flux with little conductive influence (Petrosyan et al., 2011; Spiga, 2019). Some models, however, suggest near surface heating (and drive for convection) by sensible and radiative effects to be roughly equal (Wu et al., 2021). This is because, although the radiative heat flux is greater at the surface, most passes through the lower atmosphere without being absorbed. In general, the warming of the surface and generates large near surface temperature gradients causing instabilities and, thus, intense convective turbulence.

Convective vortices and even dust devils (dust loaded convective vortices) are a commonly observed feature on Mars (Balme & Greeley, 2006; Murphy et al., 2016; Lorenz et al., 2021; Kurgansky, 2019; Hueso et al., 2022; Spiga et al., 2021). At the InSight landing site large pressure drops have been correlated a few aeolian change events but with little dust lofting (Charalambous, McClean, et al., 2021). However, most other missions including Perseverance have seen many dust devils (Newman et al., 2022; Hueso et al., 2022). On top of dust devils, convective cells have been observed to produce large dust lifting events at Perseverance which, although less frequent, likely contribute as significantly to overall aeolian transport (Newman et al., 2022).

The Martian PBL grows throughout the daytime and can reach up to $\sim$10 km. At night, however, convective motions are inhibited by surface radiative cooling which leads to the collapse of the PBL and the formation of a near surface stable layer. At this time mechanical instabilities still occur (often influenced by topography i.e. slope winds) which generate shear turbulence. The effect on turbulence of wind shear is greatest near the

surface as the wind speed generally follows a logarithmic profile with height (Monin et al., 2013), falling to zero at the surface. Chatain et al. (2021) demonstrated the evolution of turbulence over the seasons at InSight, where shear driven turbulence was shown to be heavily prevalent during the winter and less so in summer. These features are highly visible in the seismic data recorded by InSight where each type of turbulence exhibits a clear signature in the seismic noise (Charalambous, Stott, et al., 2021). Moreover, the ability to observe marsquakes is heavily modified by the seasonal evolution of turbulence.

These features of turbulence are prevalent in observed wind speed records. The Viking missions provided the first in situ records of wind speed on Mars (Hess et al., 1977). Further datasets have been acquired by the Curiosity (Gómez-Elvira et al., 2012), InSight (Banfield et al., 2019, 2020) and Perseverance missions (Rodriguez-Manfredi et al., 2021; Newman et al., 2022). The Viking missions provides hourly averaged data for 1000 sols with some more complete periods of observation. On the other hand, Curiosity suffered damage on its sensing boards upon landing and recorded data using the surviving boards with reduced quality till sol 1491, when more boards were damaged, and no further data retrieval was possible (Gómez-Elvira et al., 2014). InSight has collected wind data for over a thousand sols with an almost continuous 1 Hz sampling of the first martian year of observations. The second Martian year, however, is sparsely recorded owing to power constraints. Analysis of these wind data have proved fruitful for the understanding of turbulence in the PBL. For example, Spiga et al. (2021) demonstrated a correlation between ground temperature and turbulence to characterise the radiative control of the boundary layer. The Perseverance wind speeds were collected on a one hour on one hour off cadence and can be up to 2 Hz. However, several boards of the wind sensor were damaged due to wind-induced sand particle impacts especially during a regional dust storm on sols 313 and 315 (Hueso et al., 2022), thus hindering the wind retrieval with the same accuracy. Continued data retrieval requires wind sensor re-calibration activities.

In three dimensional fluids the turbulent energy enters the atmosphere at a source scale and generally causes eddies which continuously deconstruct into smaller eddies at the inertial scale. Finally these eddies dissipate at scales when the viscous forces acting between the particles dominate. These small scales can be investigated with high frequency measurements, which are possible to obtain with the microphone (Maurice et al., 2022). As a result, high frequency wind speed estimates obtained from the microphone provide important information on the Martian PBL.

2.2 Wind noise in microphones

Microphones, record the deviation from the ambient pressure referred to as sound pressure. As such, they are sensitive to wind fluctuations, such as those in a turbulent flow. The velocity of a wind flow, v, can be considered to be made up of two components as $v = U + u$ where U is the overall speed of the wind flow and u is the fluctuating component due to turbulence (Monin et al., 2013; Landau & Lifshitz, 2013). A fluctuating parcel of air will generate a sound wave. A given parcel of turbulence will emit a sound wave with a theoretical energy, ϵ, per unit mass and time as

$$\epsilon \sim \frac{u^8}{c^5 l}$$

where c is the speed of sound in the fluid and l is the lengthscale of the turbulent region (Landau & Lifshitz, 2013). This derivation specifically applies to a region of finite turbulence within a fluid at rest. However, a microphone will record pressure fluctuations (the dynamic pressure) which do not occur solely due to sound waves.

The empirical study of microphone noise due to wind has often been concerned with the impact of wind screens. Strasberg (1988) developed a scaling law for microphone noise depending on the Strouhal number of the wind screen. This was derived on data from low turbulence flows, collected indoors, and so the main source of noise is from the in-

teraction of the flow with the windscreen and so the pressure fluctuations recorded by the microphone are due to the wake.

Morgan and Raspet (1992) demonstrated that in outdoor recordings the noise recorded by the microphone is predominantly due to the intrinsic turbulence of the flow itself. This followed from a model based on Bernoulli's principle where the pressure fluctuations of a wind flow are related to its kinetic energy as $p = 0.5\rho(U^2 + u^2 + 2uU)$, with ρ the density and U and u the average and fluctuation velocities as above. Their experimental data showed the best correlation of microphone RMS with the uU term (where the mean and standard deviation of wind speed represented U and u respectively) with a power law between 2 and 3. Van den Berg (2006) took this further and constructed a model (with comparisons to data) for microphone wind noise based on theoretical turbulence spectra taking into account the atmospheric stability and surface roughness, verifying that microphones are able to examine the atmosphere in a broader sense.

Chide et al. (2021) characterised the effect of wind on the SuperCam microphone in a wind tunnel under Martian analogue conditions (low pressure CO_2). They found a generally quadratic relationship between the wind speed and the microphone RMS. On top of this, they found the wind incident direction contributed up to a factor of 2 difference in RMS due to induced turbulence in the wake of the SuperCam body. This was more pronounced for higher wind speed and higher frequency, generally having more impact at above 500 Hz. As these data are collected in a wind tunnel the flow is generally more laminar than outdoor winds leading to a more noticeable effect.

The effects of winds on a microphone are determined by complex processes that depend on the state of the atmosphere. This indicates that microphones can be used in two ways: (i) as wind sensors (particularly for high frequency variations) by considering the dominant impact of the wind speed where the observed sensitivity is taken as an in situ calibration and (ii) as a method to study the atmospheric state in the PBL by exploiting the detail of relationships with meteorological data. As a result, studying observed relationships between atmospheric data and a microphone is a means to study the PBL state in the first place. Comparing the atmospheric data available on the Perseverance rover to the microphone recordings will enable us to study the Martian atmosphere, in particular, the high frequency wind variations on Mars.

3 Data

3.1 Microphone recordings

Perseverance carries two microphones, one in the SuperCam instrument suite (Mimoun et al., 2022; Maurice et al., 2021) mounted on top of the remote sensing mast head 2.1 m above the ground, which can be rotated 360 degrees/pitched up and down. Another microphone bolted to the rover body (on the port side 1 m) intended to listen to the entry descent and landing, referred to as the EDL microphone (Maki et al., 2020). In this work we use only data from the SuperCam microphone as its calibration is well characterised (Mimoun et al., 2022).

Here we exploit passive microphone recordings of the martian atmosphere, where the microphone records purely the ambient sound with no simultaneous rover operations. Such recordings are typically at 25 kHz and last for 167 s. The wind-related signal itself is below 1 kHz (Maurice et al., 2021; Mimoun et al., 2022). The microphone also records the shock-waves from the LIBS shots in order to examine the properties of the rock (Murdoch et al., 2019; Chide et al., 2019, 2020). For LIBS, the microphone records at 100 kHz as the acoustic signal ranges typically from 2 kHz to 20 kHz.

An operational campaign was constructed to perform around eight 167s long (the longest possible continuous recording (Mimoun et al., 2022)) recordings at 25 kHz ev-

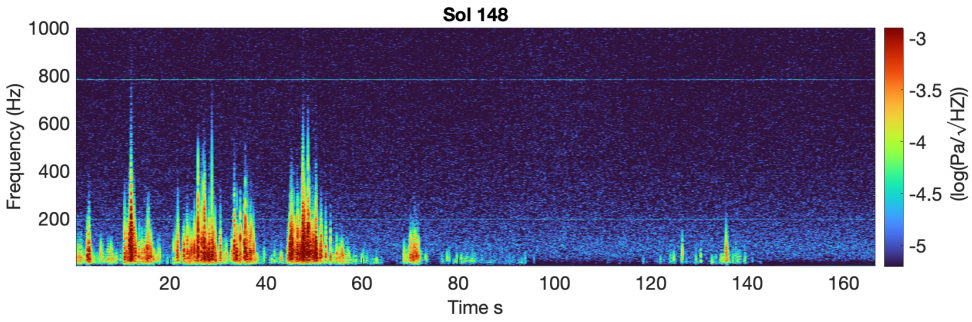

Figure 1. A spectrogram of a microphone recording taken on sol 148.

ery month. The aim was to extract the variation over the Martian sol but timings varied, for example, to prioritise day time signals (to ensure high signal to noise ratio recordings) or due to operational constraints. Another series of recordings were taken during the "360 degree spin" calibration activity. This activity took 30s long microphone recordings at different stopping angles while the SuperCam mast head was rotated through 360 degrees in order to improve the likelihood of finding any directional impact on the wind sensitivity. The general passive recordings do not have a defined pointing.

The data selected cover Ls (solar longitude) 10-260 which correspond to mission sols 0-483. We predominantly analyse the microphone signal in the 20-60 Hz bandwidth. This is because it is the region most frequently excited by the wind. As mentioned above, the wind can excite frequencies up to 1 kHz but this is uncommon and as the signal arises from the lower frequencies (they are most sensitive) we choose the lowest frequency range for the microphone. The 20-60 Hz range also ensures we do not cover too large a range to include overlapping features. The impact of wind on the microphone signal can be summarised by the RMS (root mean square) of the signal within this bandwidth. Figure 1 shows a spectrogram of an example recording on sol 148 with large gusts exciting frequencies up to 800 Hz. The lower frequencies, though, show stronger intensity (darker red) than the higher frequencies indicating the signal to have stronger lower frequency content.

3.2 Atmospheric instruments and data

Perseverance carries the Mars environmental dynamics analyser (MEDA) sensor package to measure the wind, air/surface temperatures and pressure on Mars (Rodriguez-Manfredi et al., 2021). MEDA measures five minutes at the start of each hour and also typically measures complete even/odd hours in even-/odd- numbered sols, resulting in complete coverage of the diurnal cycle every 2 sols. The wind sensor consists of two booms located 1.5m above the ground and separated by 120 degrees. Each boom provides independently measurements of wind speed and direction and the best measurement is provided by an specific algorithm calibrated on wind tunnel experiments (Rodriguez-Manfredi et al., 2021). Depending on the wind direction (which affects whether rover elements block the flow of the wind to one particular boom) one boom is selected to give the derived winds for a given period. The wind speed retrieval has a resolution of ± 0.5 m/s and accuracy of 1 m/s up to 10 m/s and resolution and accuracy of 10% of the wind speed above this. The wind direction retrieval has an accuracy of $\pm$ 15 degrees.

The pressure sensor is based on the silicon-micro-machined pressure sensor head (Barocap) and transducer technology developed by Vaisala Inc. (Rodriguez-Manfredi et al., 2021; Sanchez-Lavega et al., 2022). The MEDA PS is located inside the rover body

with an inlet that connects the sensor with the exterior. The pressure is measured with a sampling rate of 1 Hz.

Three atmospheric temperature sensors (ATS 1, 2 and 3) are located on the remote sensing mast at 1.45m and a further two (ATS 4 and 5) are located on the front of the rover at 0.85m (Rodriguez-Manfredi et al., 2021). The influence of temperature fluctuations on these sensors depends on the direction from which the air parcel comes from and also the influence of the rover. Each sensor records at up to 2 Hz and have a response to temperatures at 0.5s for wind speeds above 5 m/s while they have a response of 0.77s to temperatures at 0m/s. Details of the air temperature dataset are covered in Munguira et al. (2022).

Ground temperature, atmospheric opacity and atmospheric downwelling flux values are obtained from the thermal infrared (TIRS) sensor (Smith et al., 2022; Sebastián et al., 2020, 2021). The data recorded by the MEDA sensors enable the estimation of turbulent (sensible) heat flux. The values used in this paper are retrieved through similarity theory in Martinez et al. (2022).

4 The sensitivity of the SuperCam microphone to atmospheric data

Figure 2 (a) demonstrates the relationship between the wind speed, as measured by MEDA, and the root mean square (RMS) of the microphone signal in the 20-60 Hz frequency bandwidth. Each dot represents a 30 s section of microphone data either cut from the 167 s recordings or recorded directly in the 360 degree turn operation. This can be seen as a calibration of the microphone signal to the MEDA wind speed which can be approximated by a fourth order power law for wind speeds above 2 m/s as demonstrated. Winds below 2 m/s do not commonly generate any signal on the microphone.

Morgan and Raspet (1992) found the best correlation of the microphone signal power was with a product of the mean and standard deviation of the wind speed, where the standard deviation approximates the variable component of the wind. This relationship is examined for the SuperCam microphone in Figure 2 (b), which is also approximated by a fourth order power law. There is little difference in the level of correlation between the microphone RMS and the mean or the product of mean and standard deviation of the MEDA wind speed. This may be because the 30 s timescales are too short meaning the evaluated mean and standard deviation is not robust enough to represent the fluctuating and average components of the wind. However, using only 167 s length recordings does not show a significant change either. Note that the fourth order power law (for both Figure 2 (a) and (b)) is steeper to those found in Morgan and Raspet (1992) which are between 2-3. The wind speed does not explain all the variation in Figure 2 (a), however, and there is a significant statistical spread/variance in the correlation. The spread is also not entirely random. For example, at wind speeds between 2 and 4.5 m/s there is a cluster of recordings which does not exhibit any microphone signal power while others at the same speed do.

The statistical spread in Figure 2 (a) could be accounted for by correlations to other atmospheric data. To that end, Figure 2 (c) also shows the correlation of the microphone RMS with the wind speed, air temperature (Ta), ground temperature (Tg), the temperature gradient between air and ground (Tg-Ta) and pressure standard deviation. The diagonal of the scatter plot matrix shows the Kernel Density Estimate (KDE) of the probability density function (PDF) of each variable in order to show their distributions over the microphone recordings.

The pressure standard deviation has been shown to be well correlated to wind speed in Charalambous, Stott, et al. (2021) for InSight, and is also the case here as shown in Figure 2 (c). To that end, the correlation between the microphone RMS and pressure standard deviation shows similar features to the Figure 2 (a). In particular, the cluster

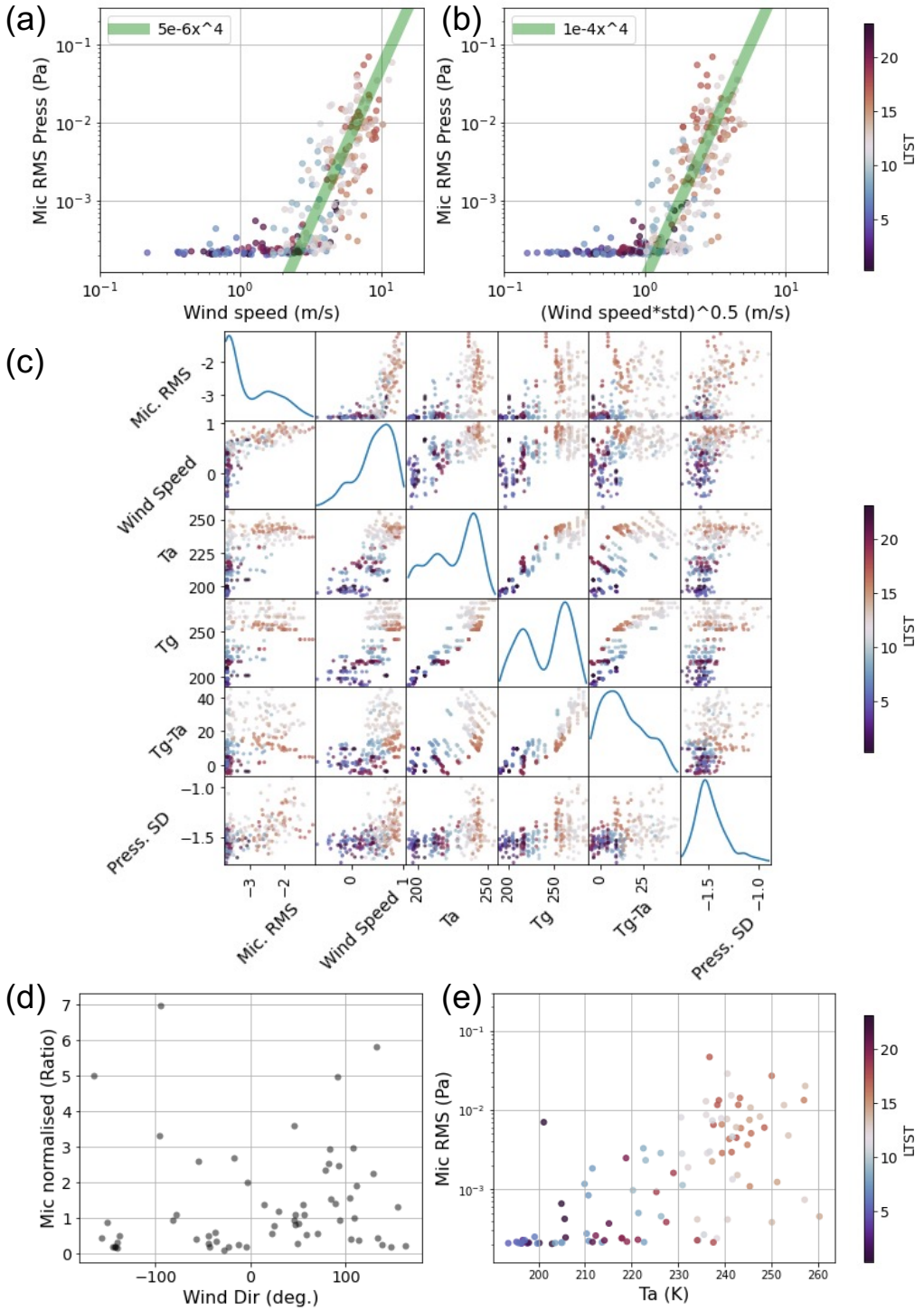

Figure 2. (a) scatter plot of the microphone RMS against mean wind speed for 30s chunks with a 4th order power law approximation shown in green. (b) scatter plot of the microphone RMS against the product of mean and standard deviation of the wind speed over 30s chunks with a 4th order power law approximation shown in green. (c) scatter plots to show correlation between key parameters (log of Mic RMS, log of wind speed, Air temperature (Ta), ground temperature (Tg) temperature gradient (Ta - Tg) and Pressure standard deviation (SD)) where each dot represents a 30s chunk of data and the diagonal plots are the KDE estimate of the PDF of each variable. (d) Incident wind direction to the microphone against the Mic RMS normalised by the power law approximation in (b) for full 167s microphone recordings with a wind speed > 3 m/s. (e) scatter plot of the microphone RMS against air temperature at 1.45m against the microphone RMS colour coded by LTST of recording.

of points with low microphone signal even though there is larger winds is more exaggerated for the pressure standard deviation. These points are typically at nighttime or late morning suggesting they are either for a more stable atmosphere (less turbulent flows which the microphone is less sensitive to) or where turbulence is less persistent and we observe a lull. This highlights that the microphone is particularly sensitive to the turbulent fluctuations, u, rather than the steady U winds.

There is a somewhat consistent relationship between the microphone RMS and the air temperature, ground temperature and ground to air temperature difference. These variables share a forcing mechanism and are, in turn, correlated to each other as shown in 2 (c). The thermal gradient, Tg-Ta, is the generative mechanism for the convective turbulent winds seen by the microphone. However, the relationship with air temperature is the most consistent and is shown in greater detail (for averages over 167s instead) in Figure 2 (e). These correlations have more of a wedge shape, rather than a simple linear correlation, suggesting that the temperatures dictate an upper bound on the signal power in the microphone data. The superior correlation with air temperature may be due to the ATS sensors which have a fast response time and their fluctuations are shown to be due to turbulence in De la Torre Juárez et al. (2022); Munguira et al. (2022). On the other hand, the ground temperature data does not fluctuate on such scales and its value depends on the surface thermal inertia and albedo, which change as the rover moves (Martinez et al., 2022). Moreover, the impact of ground temperature on the thermal gradient which impacts the wind field would be an average over the terrain.

Notice that there is an outlying black point in Figure 2 (e) with a large signal at around Ta=200 K compared to recordings at a similar temperature. This corresponds to a period of nocturnal turbulence (analysed for Perseverance in Pla Garcia (2022)) which occurred at 20 minutes after midnight local true solar time (LTST).

The MEDA wind sensor currently only determines horizontal wind speeds. This means that vertical wind speeds are not known, which would produce signal on the microphone in the same way. Vertical wind speeds are generally lower than horizontal (0.2 of the size of horizontal wind speed is used as a rule of thumb Lorenz (2022)) and are often correlated to horizontal winds. Chide et al. (2022) demonstrate an analysis of thermal fluctuations based on sound speed measurements from recordings of the LIBS shockwave. This indicates the presence of significant, fast thermal fluctuations, both vertical and horizontal.

Another aspect to investigate is the impact of wind direction. Chide et al. (2021) showed that wind incidence on the SuperCam head produced up to a factor of 2 change in the microphone signal power, owing to the wake generated. Figure 2 (d) shows the wind incidence direction (relative to the pointing direction of the microphone) against microphone RMS divided by the fourth order power law fit for recordings of wind speed above 3 m/s, with the aim of normalising the effect of wind speed. As splitting the recordings into 30s chunks provides a bias in number of data points for specific conditions (as mentioned above atmospheric stability also plays a part) we consider only the full 167s recordings along with the 30s recordings taken during the "360 degree spin" activity. The data do not demonstrate a clear pattern to suggest that wind incidence direction is important.

The observed spread in the relationship with wind speed is greater than the factor of 2 observed in Chide et al. (2021) and so other factors may obscure the effect. On top of an effect (from turbulent wake generation) of the wind incidence with the SuperCam head, additional wind directionality effects may occur due to the mast elevation or the wind incidence with the rover. For example, the Radioisotope Thermal Generator (RTG) is a source of heat, which would interfere with recordings pointing to the back of the rover. On the other hand, consider that the effect of directionality observed in Chide et al. (2021) is suggested to be due to turbulent wake induced by the SuperCam head.

According to Morgan and Raspet (1992) and Van den Berg (2006), these effects are only likely to be significant compared to the signal power from the turbulence of the flow itself when the flow has low inherent turbulence. As a result, the impact should not be as prevalent in the Martian data compared to the wind tunnel data analysed in Chide et al. (2021). Furthermore, the power law relationship to the wind speed observed on Mars is of order 4 and not the 2 found in testing, indicating a different mechanism. The 20-60 Hz bandwidth we examine is also fairly low frequency compared to the analysis in Chide et al. (2021), which indicated less sensitivity to wind direction for lower frequency signals. As a result, although some directional sensitivity cannot be ruled out, the wind direction does not provide clear information to describe the observed microphone signal from the data and it is also not expected to contribute significantly.

5 Wind speed estimation with Gaussian process regression

The goal now is to produce a wind speed estimation based on the microphone signal. In order to produce such a prediction, a calibration function must be obtained. Figure 2 (a) demonstrated a fourth order power law approximation between the microphone RMS and wind speed, which is the dominant relationship. However, there is considerable statistical spread. The air temperature was also shown to have a consistent relationship with the microphone (and indeed the wind speed) and so may explain further variance. To that end, we use both the microphone RMS and air temperature data as inputs to a calibration model for the prediction of the wind speed.

5.1 Gaussian process regression for a calibration function

Supervised machine learning techniques represent a good choice for such curve fitting problems. In this application we desire a smooth calibration function so as to propagate the signal properties of the microphone data rather than find the best fitting performance. This is because the MEDA wind sensor has its own calibration grid and we do not want to directly fit this but rather examine the different qualities/abilities from each of the respective sensors. On top of this, powerful fitting methods such as neural networks typically require several thousand data points as a minimum. As a result, we choose to implement Gaussian process (GP) regression for the task. We present a brief introduction to GP regression here and refer the reader to Williams and Rasmussen (1995) for a full review.

Gaussian processes are non-parametric, that is, they are not constrained to a functional form such as a power law. As a result, the calibration function does not suffer from artefacts due to an arbitrary construction. Instead a GP regression finds a distribution of potential functions which would fit the data as

$$\mathbf{f} \sim \mathcal{N}(\mathbf{m}, \mathbf{K}) \tag{1}$$

where $\mathbf{f}$ represents a vector of outputs of the function which is normally distributed in terms of the mean function $\mathbf{m}$ (specified as a vector and often set to zero following data normalisation) and $\mathbf{K}$ is the covariance matrix of the data. In this way, the output of the function is normally distributed.

The covariance matrix is calculated based on a kernel function, evaluated for a given input sample x with another sample x' as $k(x, x')$, where the matrix $\mathbf{K}$ consists of values of $k(x, x')$ for several input samples X. The kernel function dictates the properties (e.g. smoothness) of the potential functions which can fit the data and are designed to give a valid covariance matrix for a normal distribution as above. One such kernel function (see Williams and Rasmussen (1995) for a variety of kernel choices) is the radial basis function (RBF) given by

$$k(x, x') = \sigma^2 \exp(-\frac{\|x - x'\|^2}{2l^2})$$

where σ and l are the variance and characteristic lengthscale. These are termed hyperparameters and determine the variance and smoothness for functions dependent on the distance between inputs x and x'. These hyperparameters are optimised (through a process known as marginalisation, see Williams and Rasmussen (1995)) for a given set of training data in our case the multivariate input, denoted X, of the microphone RMS and air temperature and the output/target, denoted $\mathbf{y}$, of the corresponding observed wind speed.

The trained GP model represents a posterior distribution of functions $\mathbf{f}$ (in equation (1)) given the training data as $\mathbf{f}|X, \mathbf{y}$. To obtain a prediction for a set of new previously unseen inputs X^* we must infer from the conditional distribution $\mathbf{f}|X, \mathbf{y}, X^*$. The expected (mean) value of the distribution is taken as the prediction/estimate but distribution also yields the variance, leading to a quantification of the uncertainty of a predicted output for a new data point. In this way, the GP regression acts to interpolate the training data to provide predictions.

For our application, we trained a GP model using the GPy package (GPy, since 2012) in Python. The microphone RMS and the MEDA air temperature were chosen as inputs while the MEDA wind speed represents the output for training. An RBF was chosen as a kernel function with independent lengthscales for the microphone RMS and air temperature. The training data were the average values from 68 (80%) of the total number of 167s recordings (86). These were used to optimise the hyperparameters. The remaining 18 (20%) were used as test data to verify the fit for unseen data and ensure there is no overfitting. The trained GP model prediction for both the training and test data had a root mean square error of 1.3 m/s.

5.2 Wind speed estimates analysis

The trained GP model trained above was used to produce wind speed estimates over the available microphone recordings. To that end, the running RMS envelope was calculated for each microphone recording as a continuous input. The RMS was calculated for the microphone signal over 1 s windows with an overlap of 99% between each successive window. This represents a sample every 0.01 s and the ATS data were interpolated to match. This yields high frequency wind speed signals over each 167 s length recording.

Figure 3 (a) and (b) shows two example wind speed estimates from the GP model. The top panel of each sub figure shows the wind speed retrieval from the MEDA sensor over that period in blue and the GP prediction based on the microphone data in black with the 95% confidence interval in shaded blue. In order to show the inputs for the GP model prediction the second and third panels shows the raw microphone RMS envelope and the ATS sensor data respectively. The lowest value of the air temperature over the recording is taken as the input, which in both recordings is predominantly from ATS 1.

The first recording in Figure 3 (a) is taken around noon LTST when the surface to air thermal gradient is highest and at the height of convective activity. On the other hand, the second recording Figure 3 (b) is taken late in the afternoon after 1700 LTST just before the PBL collapses to show a contrast in conditions (Munguira et al., 2022). In both cases there is a good agreement between the microphone-based estimate and the MEDA wind speed which is almost always within the 95% confidence interval of the prediction for each example. In contrast, however, the microphone-based recordings generally exhibit sharper variations than the MEDA retrievals.

The noon recording in Figure 3 (a) shows episodic high speed gusts and low wind speed lulls. The microphone shows gusts ranging from 1-10 s in length and with wind speed peaks above 10 m/s and the confidence interval upper bound up to 14 m/s. The MEDA wind speed retrieval also shows gusts but the lengths are all of the order of 10s

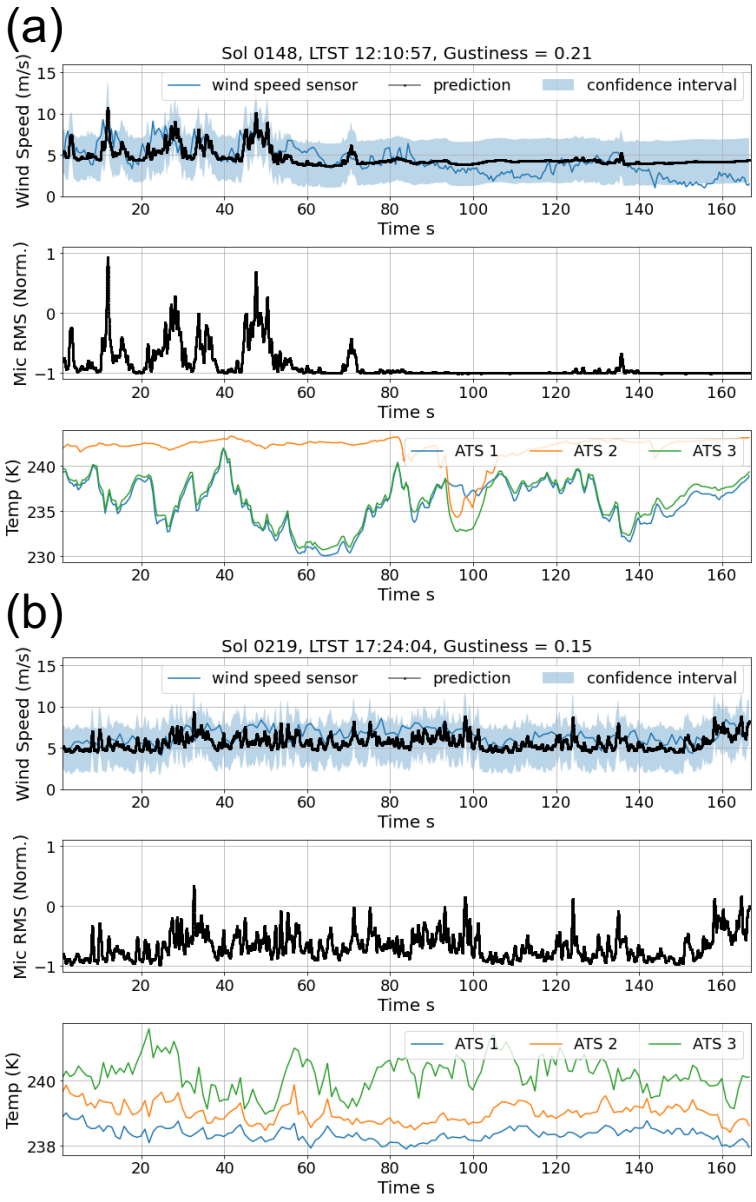

Figure 3. Wind speed estimates from the microphone and atmospheric temperature for two different recordings on sol 148 (Ls = 75) at 1210 LTST (a) and sol 219 (Ls = 107) at 1724 LTST (b). The former (a) is at the time of the largest ground to air thermal gradient with a developed PBL and the latter (b) is at the end of the afternoon just before the PBL collapse. The top panel shows the wind speed measured by MEDA (blue), the mean prediction from the GP (black) and the 95% confidence interval of the GP prediction shaded in blue. The second panel shows the RMS of the microphone signal over the recording and the bottom panel shows the raw data from ATS 1, 2 and 3, where the minimum value over the recording is used as the input to the model.

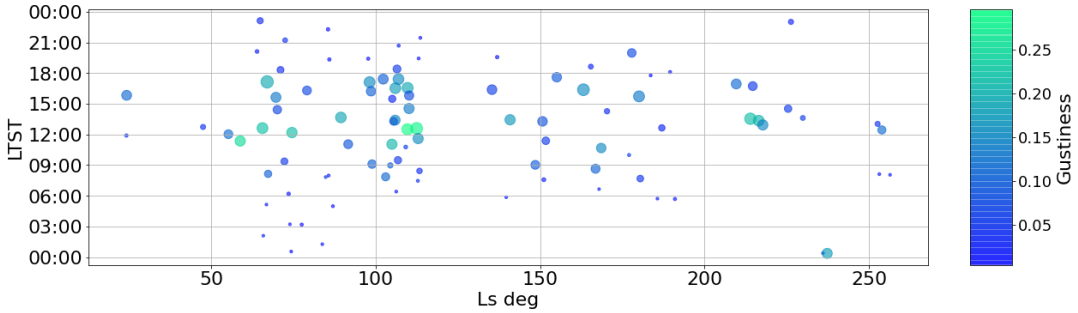

Figure 4. (a) Microphone signal power and wind speed estimate gustiness over the mission. Each dot represents a 167s microphone recording where the size of the dot is scaled according to the RMS of the recording and the colour indicates the gustiness metric for that recording.

with slightly lower peak wind speeds. During the low wind speed lulls the microphone estimate does not vary much, while the MEDA wind speed retrieval does show a slow change in wind speed magnitude. In this case, the wind variability is not enough to generate a signal on the microphone as the microphone is not very sensitive to low wind speeds, as shown in Figure 2 (a). The later afternoon recording in Figure 3 (b) has more persistent fluctuating winds, where the MEDA wind speed is always between 5-9 m/s. The microphone-based wind speed indicates a similar wind level but shows greater variability than the MEDA wind speed with shorter, sharper gusts of the order of seconds. Compared to the noon recording, however, there are no episodic gusts. The air temperature for the afternoon recording is seen to be almost constant in comparison to the air temperature at noon which shows more significant fluctuation, demonstrated by the bottom panels of Figure 3 (a) and (b) respectively.

The microphone-based estimates, therefore, are reasonable wind speed retrievals, particularly for turbulent winds. The comparison to the MEDA wind speed retrievals shows that the microphone is able to resolve short, sharp wind gusts. These gusts have a greater degree of variability than captured by MEDA, with some showing higher wind speeds for shorter periods. This helps distinguish the different qualities of the signals at noon and late afternoon shown in Figure 3, where at noon there are clear episodic gusts and lulls and late afternoon fluctuates more consistently. On the other hand, the microphone is less suitable to study low level average wind speeds. The overall level of the microphone-based estimate does reasonably match the MEDA wind speed but it is not able to follow the low level variation. This is taken into account by the GP calibration as indicated by the wide range of the confidence intervals at low wind speeds.

6 PBL turbulence with microphone wind speed estimates

6.1 Microphone wind speed gustiness

As shown in Figure 3, the microphone wind speed estimates display high frequency variations and resolves short time gusts well. The obtained wind speed estimates could therefore be used to examine turbulence in the PBL. To do so we must consider a statistic to quantify turbulence within a time series. Turbulence in wind fields refers to the variability of the flow of the wind. Gustiness is a measure of turbulent intensity which characterises the level to which a flow is turbulent. The gustiness metric is given as

$$Gustiness = \frac{\sigma}{\mu}$$

where σ and μ are the standard deviation and mean of the wind speed signal. This is effectively a measure of the variability of the wind speed time series normalised by the average wind speed, to emphasise where a signal greatly varies compared to the ambient wind speed.

This gustiness metric was calculated on the wind speed estimate produced by the GP prediction over each 167s microphone recording. Figure 4 shows the ambient microphone recordings from across the mission to date where each dot represents a recording at a particular LTST and Ls. The size of the dot is scaled to represent the RMS of the microphone signal and the colour encodes the gustiness of that recording. It can be seen that strong signal power (large RMS), and therefore strong winds, typically occur throughout the afternoon. However, this is not always coincident with strong gustiness values which tend to occur earlier in the sol from 9-13 LTST. This is consistent with Chide et al. (2022) who demonstrate that sound speed derived thermal fluctuations are greatest at this time. The wind earlier on appears more episodic where there is a mix of small and large signal power recordings. On the other hand, the later wind is more consistently strong with few small dots, low signal recordings, in the mid afternoon period.

6.2 Comparison to vortex rates

Pressure drops are another marker of pressure oscillations. Hueso et al. (2022) has provided a catalogue of pressure drops >0.3 Pa for the first 415 sols of the mission. In Figure 5 (a) we show a histogram for the number of pressure drops detected within each LTST hour compared to each gustiness value calculated on the microphone wind speed estimate. The pressure drop rates are generally low during the night time and pick up from 10 LTST, peaking at noon and dying down after 17 LTST. The overall distribution of gustiness is a close match to the pressure drop rates but the gustiness has slightly heavier tails over a broader range, increasing from the nighttime lows around 7 LTST and dying off at 18 LTST. The nocturnal turbulence recording mentioned above stands out with a high gustiness (around 0.17) just after midnight.

As mentioned the 167s length is too short to necessarily be a robust representation of the period but the distribution of these values indicates the variation of the episodic gusts. To that end, Figure 5 (c) quantifies the distribution of gustiness from the microphone for four hour periods over the sol. This violin plot shows the KDE estimate of the PDF of values vertically. Figure 5 (b) instead shows the distribution of the logarithm of the pressure drops size for the same four hour periods. Within each violin a horizontal line represents an individual observation, indicating the relative lack of observations for the microphone compared to the ability of the continuous measurements of pressure to assess the pressure drop rate. Despite this, similarities can be observed between the distributions particularly during the day time. This comparison verifies that the high frequency wind estimates from the microphone data are suitable to assess turbulence, particularly at small scales.

6.3 Thermal correlations with gustiness

Buoyancy generated turbulence occurs due to atmospheric instability from thermal imbalances. To that end, the correlation of the gustiness metric with the various temperature data recorded by Perseverance is of interest to examine the behaviour and control of turbulence in the PBL. Figure 6 (a) shows scatter plots of the gustiness metric for the microphone wind speed against the same metric on the MEDA wind speed data, the wind speed data itself, air temperature, ground temperature, the ground - air temperature difference (gradient) and turbulent heat flux. On the diagonal of the scatter plots matrix is the KDE estimate of the PDF of each variable to show their respective distributions.

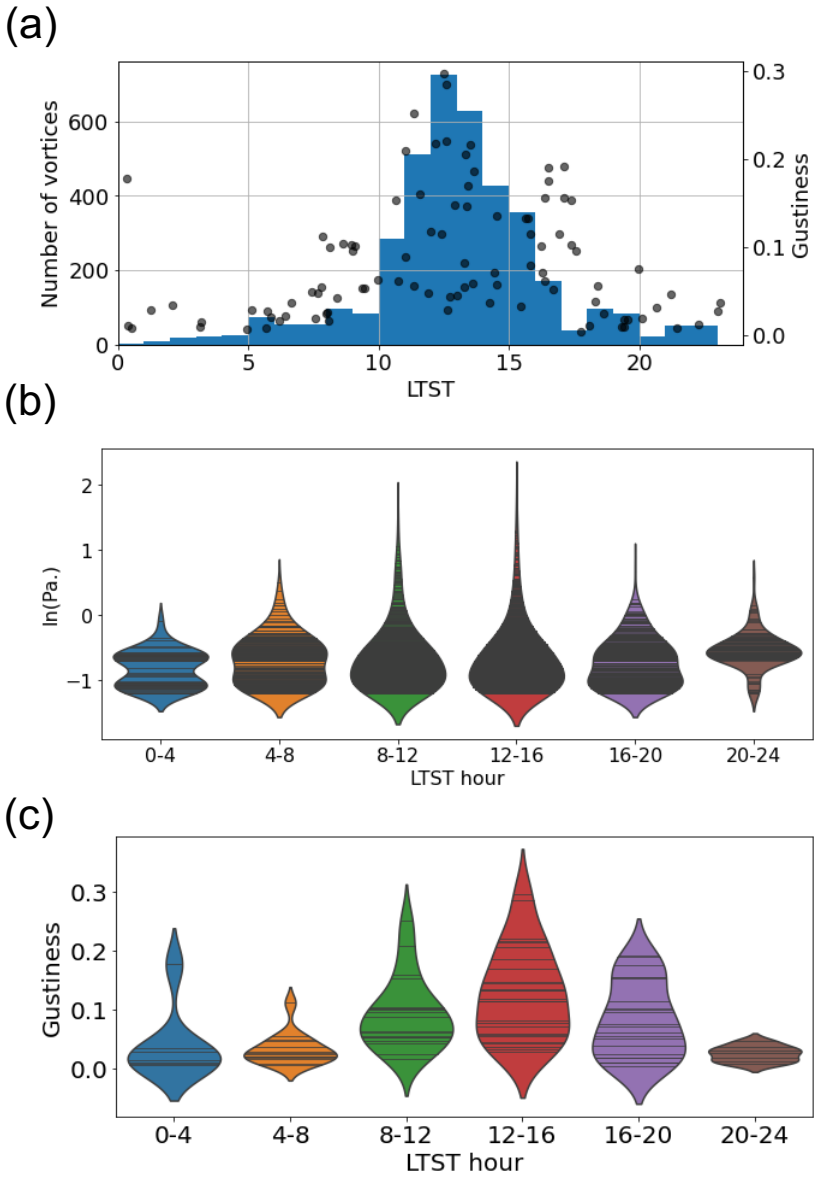

Figure 5. (a) histogram of number of pressure drops >0.3 Pa each LTST hour and gustiness of each 167s microphone recording at the LTST it occured. (b) violin plot of pressure drops (in terms of ln(Pa)) for four LTST hour groups. (c) violin plot of gustiness for four LTST hour groups.

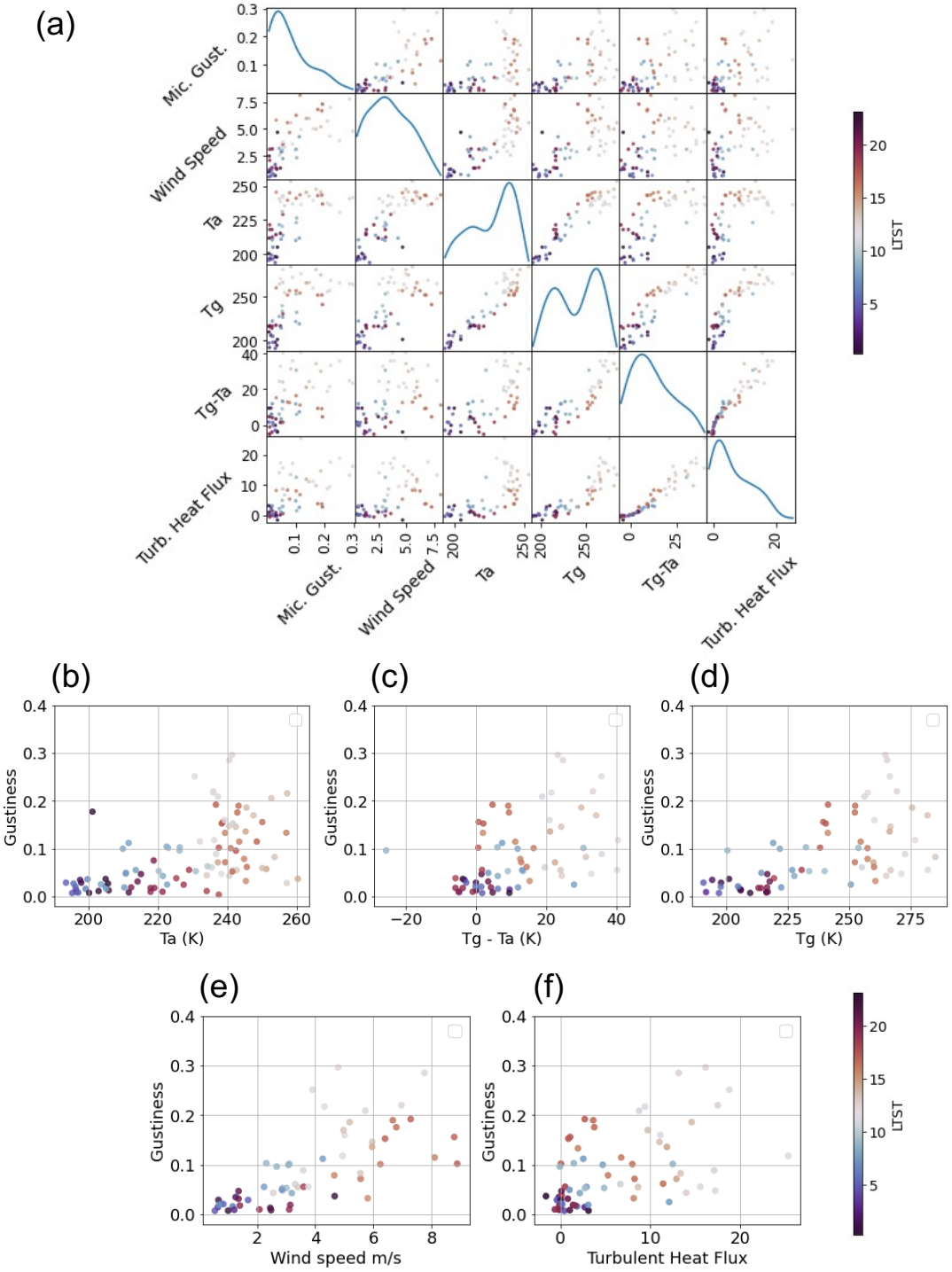

Figure 6. (a) A scatter plot matrix to show correlations between the microphone gustiness, air temperature (Ta), temperature gradient (ground (Tg) - air (Ta) temperature), ground temperature (Tg), wind speed and turbulent heat flux where each dot corresponds to a single 167 s recording. The diagonal of the matrix shows a KDE estimate of the variable PDF. (b)–(f) a scatter plot of each key parameter against the gustiness for the microphone wind speed estimate for each 167s recording.

The relationships between gustiness and air temperature, ground temperature, temperature gradient, wind speed and turbulent heat flux are each shown in more detail in Figures 6 (b)-(f). Each plot shows some positive correlation, albeit with a large spread/variance. It is important to note that these factors are somewhat degenerate, as shown by their respective correlation in Figure 6 (a), which makes establishing the dominant effects difficult.

The temperature difference between the air and ground is an indication of atmospheric instability. This implies that higher temperature gradients (in particular when the ground is warmer than the air) should generate more intense turbulence. Figure 6 (c) does show that larger gradients do tend to have higher gustiness, although with significant (and increasing) variance. Munguira et al. (2022) and De la Torre Juárez et al. (2022) report a correlation between atmospheric temperature standard deviation (indicating turbulence) and this gradient, thus, in agreement with our findings. They demonstrate a relatively strong correlation during the unstable part of the sol and a weaker reversed correlation for more stable conditions. The microphone gustiness also demonstrates evidence of a separate cluster for the stable periods, demonstrated in Figure 6 (c) by the darker coloured points (corresponding to early morning or late afternoon LTSTs) with low gustiness values around 0 K.

The overall variation of the PBL is predominantly driven by radiative flux which raises the ground temperature. This drives the instability (thermal gradient) in the PBL giving rise to buoyancy driven turbulence. Spiga et al. (2021) demonstrated that ground temperature is indeed the best explanatory variable for wind gustiness at InSight, verifying the radiative control. We also find a positive correlation, shown in Figure 6 (d), in agreement with these findings. The correlation to ground temperature has an increasing variance with increasing ground temperature, that is, it is heteroscedastic. A similar observation can also be made in Figure 12 of Spiga et al. (2021). This increasing variance (heteroscedasticity) is also occurring in many of the other demonstrated correlations.

A similar correlation with air temperature is also demonstrated in Figure 6 (b). The air temperature plot contains more data points as more coincident air temperature data was available at the point of writing. Notice that the nocturnal turbulence (black dot with gustiness = 0.17) appears as an outlier compared to atmospheric temperature, in agreement with it being due to shear rather than buoyancy. The ground temperature data for this recording was not available for comparison.

As mentioned, the analysis of Spiga et al. (2021) was performed on averages between 11-14 LTST over the Martian season. On the other hand, our analysis is for short 167 s signals taken from across the entire sol. As a result, we cannot straightforwardly decouple diurnal and seasonal factors. This is highlighted by comparing our correlation to turbulent heat flux (in Figure 6 (f)) to that in Spiga et al. (2021). We show a general increase in gustiness with turbulent heat flux (most clearly for < 5 W/m^2) but Spiga et al. (2021) show a negative correlation. As their analysis is produced for the seasonal evolution of the daytime (11-14 LTST) PBL the range of turbulent heat flux examined is 12-33 W/m^2, while we only show a few points in this range. Above ~ 10 W/m^2, Figure 6 (f) does not in fact show clear correlation, while the majority of points below 10 W/m^2 with a more positive correlation are later afternoon to early morning, outside the period examined by Spiga et al. (2021).

Figure 6 (e) shows a positive correlation between wind speed and gustiness. Despite our apparent correlation, high wind speeds have been posited to inhibit turbulence. There is some indication that noon values (lighter dots) have large turbulent intensity at lower winds speeds, while the late afternoon (red dots) show weaker gustiness for the larger values of wind speed. However, there are not enough data points to draw this con-

clusion. Moreover, we only observe mean wind speeds up to 10 m/s and so may not observe this effect clearly.

6.4 Atmospheric dust content correlation with gustiness

Dust particles suspended in the Martian atmosphere have significant radiative and dynamical effects on the Martian atmosphere due to their absorption of solar radiation and their contribution to radiative fluxes in thermal infrared wavelengths (e.g., Madeleine et al. (2011)). A dustier atmosphere on Mars has often been believed to increase the surface shading by suspended dust particles and therefore weaken the turbulence in the planetary boundary layer (see review by Spiga (2019)), which then leads to a negative feedback for dust lifting (Kahre et al., 2006; Newman et al., 2002). This, however, assumes an even distribution of dust in the atmosphere. On the contrary, Wu et al. (2021) reported turbulence-resolving numerical simulations able to transport dust actively in the turbulent motions resolved by their model and to examine the feedback processes between turbulent dust mixing and radiative effects. They found that the lofting of dust through convective plumes causes an inhomogenous distribution of the warm dust particles in the atmosphere which promotes thermal instabilities and results in stronger turbulence in the planetary boundary layer. In their model, this effect of inhomogenous dust distribution is particularly effective for low to moderate dust loading with several active areas of dust lifting from the surface.

In this section, we intend to explore whether our dataset could provide more insight into this process and the feedback between dust loading and turbulence in the PBL. In fact, the atmospheric conditions in Jezero crater during the first part of the Mars 2020 mission are optimal to compare with the Wu et al. (2021) model results, since dust loading has been low to moderate and since many dust lifting events have been observed (Newman et al., 2022). We compare our dataset to regular measurements of aerosol opacity (tau) and to the downwelling atmospheric IR flux (LWd) acquired by the TIRS instrument on Perseverance, described in Smith et al. (2022). The relationship between the microphone gustiness and the obtained opacity and downwelling atmospheric IR flux data are shown in Figure 7.

The downwelling atmospheric flux is shown (in the scatter plot matrix in Figure 7 (a)) to be correlated with the air temperature and, in turn, many of the relationships highlighted above in Figure 6. There is therefore a positive correlation with gustiness. In particular, there is a fairly sharp increase for values 15-20 W/m^2. There are a few recordings with LWd above 20 W/m^2 with a large range of corresponding gustiness. Notice that the recording corresponding to a period of nocturnal turbulence (the black dot with gustiness around 0.17) appears inline with this relationship rather than as an outlier as was the case with atmospheric temperature in Figure 6 (b).

The effects of dust loading on turbulence suggested by Wu et al. (2021) occur over a relatively large scale compared to our observations and are due to the non-uniformity of dust distribution within the convective structures. The timescales involved for dust heterogeneity in the PBL are therefore of a few minutes but the timescales involved for a change of the mean dust optical depth over an area is of a few hours. Here we compare the gustiness metric with the mean value of optical depth measured by Perseverance from the preceding 6 hours and the standard deviation of optical depth taken from the preceding 6 hours and 2 sols. These statistics of opacity do not correlate clearly with the air temperature and hence provides a contrast to the other factors examined so far.

Figure 7 (b) shows that there is some positive, curve shaped, correlation with the value of gustiness and mean value of opacity. This is most evident as an upper bound for noon-afternoon (light and red dots) recordings with an average opacity in the range 0-0.3. The evening, nighttime and morning recordings do not correlate as well for the same values of opacity, which may be because they are not in the convective period. There

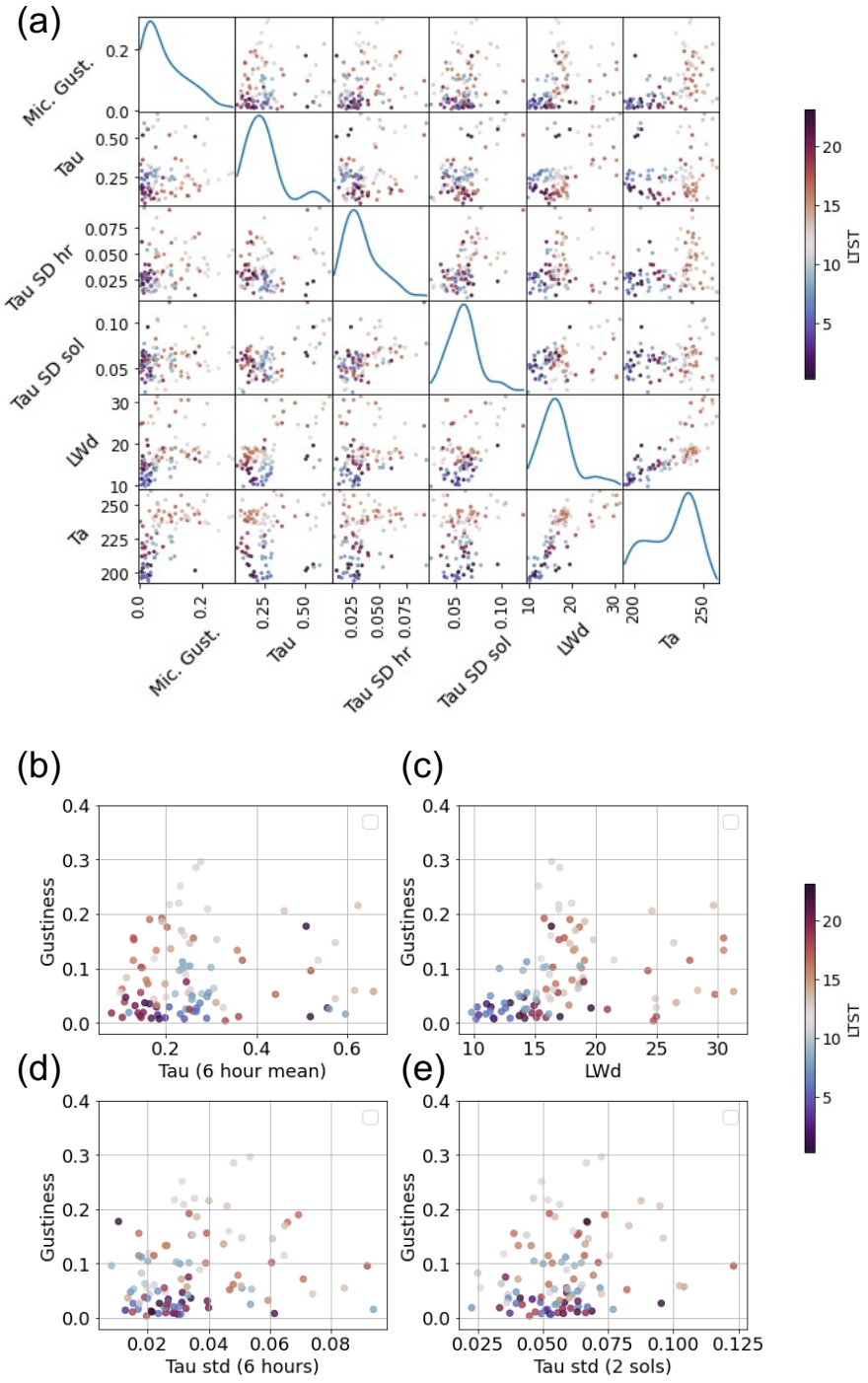

Figure 7. (a) A scatter plot matrix to show correlations between the microphone gustiness, aerosol opacity averaged over 6 hours (tau), downwelling atmospheric IR flux (LWd), the standard deviation of opacity for the preceding 6 hours (tau SD hr) and 2 sols (tau SD sol) along with air temperature (Ta). Each dot corresponds to a single 167 s recording and the diagonal of the matrix shows a KDE estimate of the variable PDF. (b)–(e) a scatter plot of each variable to the microphone gustiness.

are a few recordings for higher values of opacity above 0.4 which exhibit a large variance of gustiness, one of which is the nocturnal turbulence recording.

Figures 7 (d) and (e) show the relationship between gustiness and the standard deviation of opacity evaluated on the previous 6 hours and 2 sols respectively to highlight the effect of variation in opacity over different scales on the turbulent intensity. In both cases the increase in standard deviation tends to cause an increase in gustiness, particularly through looking at the daytime recordings during the convective period. This breaks down somewhat for higher standard deviations (above 0.05 and 0.075 in the 6 hours and 2 sols data respectively) where the gustiness is lower. In comparison to the 6 hour time scale, the 2 sol standard deviation has fewer values outside of the main grouping, particularly at higher values of standard deviations as well as the nocturnal turbulence value not being an outlier. This demonstrates that both long term and short term variation in opacity could contribute. The correlations between the gustiness metric and mean/standard deviation of opacity are therefore consistent with the role of dust in increasing turbulence proposed by Wu et al. (2021) to some extent. However, further analysis is required to isolate the particular effects.

7 Discussion and conclusion

This paper provides high frequency wind estimates from Mars using the SuperCam microphone on Perseverance. These wind estimates are based on the demonstrated relationships between the microphone RMS and the air temperature for the Perseverance data. The dominant relationship is with the wind speed, which can be approximated with a fourth order power law above 2 m/s. This correlation, however, has significant statistical spread/variance and substructure which can be due to several unobserved factors (e.g. vertical winds) and due to short recording lengths. Further information to explain the variance in the correlation is given by the atmospheric data. In particular, the air temperature data gives an upper bound on the microphone RMS. The way in which the atmospheric stability affects the microphone data is important to take into account when using the microphone to study the wind.

The GP calibration yields a suitable method to obtain wind speed estimates based on the microphone RMS and air temperature data as it acts to interpolate the observed relationships between the microphone and wind data. This allows the output to exhibit the high frequency variation observed by the microphone rather than trying to overly fit and reproduce the MEDA wind speed retrieval. The non-parametric form of the GP model allows for variation in the calibration function to be taken into account, not strictly confining to the form of a power law which is only shown to work in general. The confidence intervals give an intrinsic understanding of the quality of the wind speed estimation.

From the comparison of the MEDA and microphone-based wind speed time series, we demonstrate that the microphone yields sharp fluctuations on shorter time scales than possible for the MEDA wind speed sampling and therefore, information on high frequency variation in the Martian atmosphere. This follows from the sensitivity analysis and prior works where the microphone is more sensitive to the turbulent fluctuations, u, and so the derived wind estimate is most suitable for their analysis at high frequencies.

The microphone-based estimate reveals episodic gusts on the 1-10 s scales with temporarily high speeds, the distribution of which appears to change over the sol. Owing to this gust resolving feature, the microphone wind speed estimate can be used to analyse specific signals such as those made by dust devils (Murdoch et al., 2021). Furthermore, the fine gust resolution can be used to examine the distribution of high wind speeds in turbulent conditions. The range of possible winds is well quantified also by the confidence intervals of the GP model. The microphone wind speed estimates can therefore

identify periods where particle lofting thresholds could have been broken (Charalambous, McClean, et al., 2021), especially for short periods. Moreover, the distributions help characterise the variability of winds which has been proposed to be a factor in aeolian process activity (Newman et al., 2022).

The high frequency sampling and gust resolving qualities make the microphone wind estimates advantageous to analyse turbulence, whereby we are able to observe the effects of small scale eddies. To that end, we calculated the gustiness metric as a marker of turbulent intensity which was compared to pressure drop rates and other meteorological data recorded by the Perseverance mission. These gustiness values obtained from the microphone wind speed estimates incorporate both diurnal and seasonal effects and also only calculated over a relatively short time period. The short timescales mean that a particular recording may not necessarily be representative of the PBL behaviour at that time, for example, an entire recording could be during a lull in the normally gusty period around noon. However, the distribution of gustiness values can help characterise the episodic nature. Recall also that Perseverance moves over ground with varying thermal inertia and albedo, which in turn affects the ground temperature value. The impact of this on the wind field would be an average over the area, making the recorded temperature value perhaps not representative either. These factors each add to the large variance demonstrated by the correlations and prohibit a statistically robust determination of the driving factors, an already difficult task given the complexity of the stochastic system and where many of the variables are correlated to each other.

Nevertheless, the correlations do represent a useful snapshot of PBL activity. Our main observations are:

1. The gustiness values are distributed over the sol similarly to pressure drops in terms of rates and sizes.
2. The gustiness is positively correlated with ground temperature, consistent with the radiative forcing of the PBL and conclusions of Spiga et al. (2021).
3. Observations 1 and 2 verify that the gustiness values obtained from the high frequency microphone wind speed estimates are reasonable estimates of turbulent intensity.
4. The gustiness values tend to increase for an increase in the ground - air temperature gradient, indicating the effect of day time atmospheric instability and convection.
5. There is a positive correlation between the gustiness and wind speed and air temperature and a more complex increase for the lower range of turbulent heat flux.
6. We have found a possible correlation between the mean and standard deviation of atmospheric opacity and gustiness. This is particularly true for afternoon recordings during the convective period consistent with the model proposed by Wu et al. (2021).
7. The relationships all show a heteroscedastic variance (an increasing variance with the variable). This is in part due to the short period over which the statistic is evaluated but it helps to characterise the variability at these scales, also captured in the distributional analysis in Figure 5.
8. We observe a nocturnal turbulence recording which does not fit to the relationships with temperature (it is not convective turbulence) but is consistent with a relationship to downwelling atmospheric IR flux and opacity standard deviation over the preceding 2 sols.

The suggestion of a possible link between optical opacity and turbulent intensity with in situ data is particularly intriguing in the context of the results of Wu et al. (2021), however, as mentioned care should be taken with drawing conclusions. In order to make more robust inferences more data over a complete Martian year and a joint analysis with

the more continuously sampled MEDA wind, pressure and temperature data is required. This continuous analysis would provide context to specific microphone observations and aid the uncoupling of diurnal and seasonal variation. This is demonstrated in Figure 5 where the distributions of the gustiness metric show links with the more complete pressure drop data, while indicating the current lack of density in microphone recordings.

This work represents a first analysis of high frequency wind speeds retrieved from a microphone on Mars. To that end, the correlations of gustiness with various meteorological data provides a statistical characterisation of turbulent intensity in the Martian PBL. This can be used to compare to existing PBL models. Future work with a larger data set is required to extract particular features of the high frequency winds, towards defining the behaviour of the dissipative regime on Mars.

Acknowledgments

We are grateful to the many people who helped with this project (in addition to the co-authors) including hardware and operations teams. In France, this project is conducted under the authority of CNES. Part of this research was carried out at the Jet Propulsion Laboratory, California Institute of Technology, under a contract with the National Aeronautics and Space Administration (80NM0018D0004). The US-based coauthors, acknowledge sponsorship from NASA's Mars 2020 project, the Game Changing Development program within the Space Technology Mission Directorate and from the Human Exploration and Operations Directorate. The UPV/EHU team (Spain) is supported by Grant PID2019-109467GB-I00 funded by 1042 MCIN/AEI/10.13039/501100011033/ and by Grupos Gobierno Vasco IT1742-22.

Data Availability

All Mars 2020 MEDA data necessary to reproduce each figure shown in this manuscript are available via the Planetary Data System (PDS) Atmospheres node (DOI: 10.17189/1522849). All acoustic data are publicly available at the Planetary Data System Geosciences Node. https://doi.org/10.17189/1522646

References

Balme, M., & Greeley, R. (2006). Dust devils on earth and mars. *Reviews of Geophysics*, *44*(3).

Banfield, D., Rodriguez-Manfredi, J., Russell, C., Rowe, K., Leneman, D., Lai, H., ... others (2019). Insight auxiliary payload sensor suite (apss). *Space Science Reviews*, *215*(1), 1–33.

Banfield, D., Spiga, A., Newman, C., Forget, F., Lemmon, M., Lorenz, R., ... others (2020). The atmosphere of mars as observed by insight. *Nature Geoscience*, *13*(3), 190–198.

Charalambous, C., McClean, J., Baker, M., Pike, W., Golombek, M., Lemmon, M., ... others (2021). Vortex-dominated aeolian activity at insight's landing site, part 1: Multi-instrument observations, analysis, and implications. *Journal of Geophysical Research: Planets*, *126*(6), e2020JE006757.

Charalambous, C., Stott, A. E., Pike, W., McClean, J. B., Warren, T., Spiga, A., ... others (2021). A comodulation analysis of atmospheric energy injection into the ground motion at insight, mars. *Journal of Geophysical Research: Planets*, *126*(4), e2020JE006538.

Chatain, A., Spiga, A., Banfield, D., Forget, F., & Murdoch, N. (2021). Seasonal variability of the daytime and nighttime atmospheric turbulence experienced by insight on mars. *Geophysical Research Letters*, *48*(22), e2021GL095453.

Chide, B., Maurice, S., Cousin, A., Bousquet, B., Mimoun, D., Beyssac, O., ...

Wiens, R. C. (2020). Recording laser-induced sparks on mars with the supercam microphone. *Spectrochimica Acta Part B: Atomic Spectroscopy*, *174*, 106000.

Chide, B., Maurice, S., Murdoch, N., Lasue, J., Bousquet, B., Jacob, X., ... others (2019). Listening to laser sparks: a link between laser-induced breakdown spectroscopy, acoustic measurements and crater morphology. *Spectrochimica Acta Part B: Atomic Spectroscopy*, *153*, 50–60.

Chide, B., Murdoch, N., Bury, Y., Maurice, S., Jacob, X., Merrison, J. P., ... others (2021). Experimental wind characterization with the supercam microphone under a simulated martian atmosphere. *Icarus*, *354*, 114060.

Chide, B., et al. (2022). Acoustics reveals short-term air temperature fluctuations near mars' surface. *This issue*.

De la Torre Juárez, M., et al. (2022). The diurnal cycle of temperature fluctuations at jezero crater. *JGR: Planets*.

Dundas, C. M., Becerra, P., Byrne, S., Chojnacki, M., Daubar, I. J., Diniega, S., ... others (2021). Active mars: A dynamic world. *Journal of Geophysical Research: Planets*, *126*(8), e2021JE006876.

Farley, K. A., Williford, K. H., Stack, K. M., Bhartia, R., Chen, A., de la Torre, M., ... others (2020). Mars 2020 mission overview. *Space Science Reviews*, *216*(8), 1–41.

Gómez-Elvira, J., Armiens, C., Carrasco, I., Genzer, M., Gómez, F., Haberle, R., ... others (2014). Curiosity's rover environmental monitoring station: Overview of the first 100 sols. *Journal of Geophysical Research: Planets*, *119*(7), 1680–1688.

Gómez-Elvira, J., Armiens, C., Castañer, L., Domínguez, M., Genzer, M., Gómez, F., ... others (2012). Rems: The environmental sensor suite for the mars science laboratory rover. *Space science reviews*, *170*(1), 583–640.

GPy. (since 2012). *GPy: A gaussian process framework in python.* `http://github.com/SheffieldML/GPy`.

Hess, S., Henry, R., Leovy, C. B., Ryan, J., & Tillman, J. E. (1977). Meteorological results from the surface of mars: Viking 1 and 2. *Journal of Geophysical Research*, *82*(28), 4559–4574.

Hueso, R., et al. (2022). Convective vortices and dust devils detected and characterised by mars 2020. *this issue*.

Kahre, M. A., Murphy, J. R., & Haberle, R. M. (2006). Modeling the martian dust cycle and surface dust reservoirs with the nasa ames general circulation model. *Journal of Geophysical Research: Planets*, *111*(E6).

Kurgansky, M. (2019). On the statistical distribution of pressure drops in convective vortices: Applications to martian dust devils. *Icarus*, *317*, 209–214.

Landau, L. D., & Lifshitz, E. M. (2013). *Fluid mechanics: Landau and lifshitz: Course of theoretical physics, volume 6* (Vol. 6). Elsevier.

Lorenz, R. D. (2022). Turbulence for extraterrestrial aviation: Gust specification for dragonfly's powered flights. *Planetary and Space Science*, *214*, 105459.

Lorenz, R. D., Spiga, A., Lognonne, P., Plasman, M., Newman, C. E., & Charalambous, C. (2021). The whirlwinds of elysium: A catalog and meteorological characteristics of "dust devil" vortices observed by insight on mars. *Icarus*, *355*, 114119.

Madeleine, J.-B., Forget, F., Millour, E., Montabone, L., & Wolff, M. (2011). Revisiting the radiative impact of dust on mars using the lmd global climate model. *Journal of Geophysical Research: Planets*, *116*(E11).

Maki, J., Gruel, D., McKinney, C., Ravine, M., Morales, M., Lee, D., ... others (2020). The mars 2020 engineering cameras and microphone on the perseverance rover: A next-generation imaging system for mars exploration. *Space Science Reviews*, *216*(8), 1–48.

Mangold, N., Gupta, S., Gasnault, O., Dromart, G., Tarnas, J., Sholes, S., ... oth-

ers (2021). Perseverance rover reveals an ancient delta-lake system and flood deposits at jezero crater, mars. *Science*, *374*(6568), 711–717.

Martinez, G., et al. (2022). Surface energy budget, albedo and thermal inertia at jezero crater, mars, as observed from the mars 2020 meda instrument. *This issue*.

Maurice, S., Chide, B., Murdoch, N., Lorenz, R. D., Mimoun, D., Wiens, R. C., ... others (2022). In situ recording of mars soundscape. *Nature*, *605*(7911), 653–658.

Maurice, S., Wiens, R. C., Bernardi, P., Caïs, P., Robinson, S., Nelson, T., ... others (2021). The supercam instrument suite on the mars 2020 rover: Science objectives and mast-unit description. *Space Science Reviews*, *217*(3), 1–108.

Mimoun, D., Cadu, A., Murdoch, N., Sournac, A., Parot, Y., Bernardi, P., ... others (2022). The mars microphone onboard supercam. *arXiv preprint arXiv:2208.01940*.

Monin, A., Sergeevich, & Yaglom, A. M. (2013). *Statistical fluid mechanics, volume ii: mechanics of turbulence* (Vol. 2). Courier Corporation.

Morgan, S., & Raspet, R. (1992). Investigation of the mechanisms of low-frequency wind noise generation outdoors. *The Journal of the Acoustical Society of America*, *92*(2), 1180–1183.

Munguira, A., et al. (2022). Near surface atmospheric temperatures at jezero from mars 2020 meda measurements. *This issue*.

Murdoch, N., Chide, B., Lasue, J., Cadu, A., Sournac, A., Bassas-Portús, M., ... others (2019). Laser-induced breakdown spectroscopy acoustic testing of the mars 2020 microphone. *Planetary and Space Science*, *165*, 260–271.

Murdoch, N., Lorenz, R., Chide, B., Cadu, A., Stott, A., Maurice, S., ... Mimoun, D. (2021). Predicting signatures of dust devils recorded by the supercam microphone. n. In *52nd lunar and planetary science conference* (p. 1658).

Murphy, J., Steakley, K., Balme, M., Deprez, G., Esposito, F., Kahanpää, H., ... others (2016). Field measurements of terrestrial and martian dust devils. *Space Science Reviews*, *203*(1), 39–87.

Newman, C. E., Hueso, R., Lemmon, M. T., Munguira, A., Vicente-Retortillo, Á., Apestigue, V., ... others (2022). The dynamic atmospheric and aeolian environment of jezero crater, mars. *Science Advances*, *8*(21), eabn3783.

Newman, C. E., Lewis, S. R., Read, P. L., & Forget, F. (2002). Modeling the martian dust cycle, 1. representations of dust transport processes. *Journal of Geophysical Research: Planets*, *107*(E12), 6–1.

Petrosyan, A., Galperin, B., Larsen, S. E., Lewis, S., Määttänen, A., Read, P., ... others (2011). The martian atmospheric boundary layer. *Reviews of Geophysics*, *49*(3).

Pla Garcia, J. (2022). Nocturnal turbulence at jezero driven by the onset of a low-level jet as determined from meda measurements and modeling. *this issue*.

Read, P., Galperin, B., Larsen, S. E., Lewis, S. R., Määttänen, A., Petrosyan, A., ... et al. (2017). The martian planetary boundary layer. In R. M. Haberle, R. T. Clancy, F. Forget, M. D. Smith, & R. W. Zurek (Eds.), *The atmosphere and climate of mars* (p. 172–202). Cambridge University Press. doi: 10.1017/9781139060172.007

Read, P., Lewis, S., & Mulholland, D. (2015). The physics of martian weather and climate: a review. *Reports on Progress in Physics*, *78*(12), 125901.

Rodriguez-Manfredi, J. A., De la Torre Juárez, M., Alonso, A., Apéstigue, V., Arruego, I., Atienza, T., ... others (2021). The mars environmental dynamics analyzer, meda. a suite of environmental sensors for the mars 2020 mission. *Space science reviews*, *217*(3), 1–86.

Sanchez-Lavega, A., T, d. R.-G., R, H., M, d. l. T. J., et al. (2022). Mars 2020 perseverance rover studies of the atmosphere over jezero from pressure measurements. *this issue*.

Sebastián, E., Martínez, G., Ramos, M., Haenschke, F., Ferrándiz, R., Fernández, M., & Manfredi, J. A. R. (2020). Radiometric and angular calibration tests for the meda-tirs radiometer onboard nasa's mars 2020 mission. *Measurement*, *164*, 107968.

Sebastián, E., Martínez, G., Ramos, M., Perez-Grande, I., Sobrado, J., & Manfredi, J. A. R. (2021). Thermal calibration of the meda-tirs radiometer onboard nasa's perseverance rover. *Acta Astronautica*, *182*, 144–159.

Smith, M., et al. (2022). Diurnal and seasonal variations of aerosol optical depth observed by meda/tirs at jezero crater, mars. *this issue*.

Spiga, A. (2019). The planetary boundary layer of mars. In *Oxford research encyclopedia of planetary science*.

Spiga, A., Murdoch, N., Lorenz, R., Forget, F., Newman, C., Rodriguez, S., ... others (2021). A study of daytime convective vortices and turbulence in the martian planetary boundary layer based on half-a-year of insight atmospheric measurements and large-eddy simulations. *Journal of Geophysical Research: Planets*, *126*(1), e2020JE006511.

Strasberg, M. (1988). Dimensional analysis of windscreen noise. *The Journal of the Acoustical Society of America*, *83*(2), 544–548.

Van den Berg, G. (2006). Wind-induced noise in a screened microphone. *The Journal of the Acoustical Society of America*, *119*(2), 824–833.

Wang, H., & Richardson, M. I. (2015). The origin, evolution, and trajectory of large dust storms on mars during mars years 24–30 (1999–2011). *Icarus*, *251*, 112–127.

Williams, C., & Rasmussen, C. (1995). Gaussian processes for regression. *Advances in neural information processing systems*, *8*.

Wu, Z., Richardson, M. I., Zhang, X., Cui, J., Heavens, N. G., Lee, C., ... others (2021). Large eddy simulations of the dusty martian convective boundary layer with marswrf. *Journal of Geophysical Research: Planets*, *126*(9), e2020JE006752.

Zurek, R. W., & Martin, L. J. (1993). Interannual variability of planet-encircling dust storms on mars. *Journal of Geophysical Research: Planets*, *98*(E2), 3247–3259.